Volume 2
Number 9
7 May 2021
Pages 2763–3122

Materials Advances

rsc.li/materials-advances

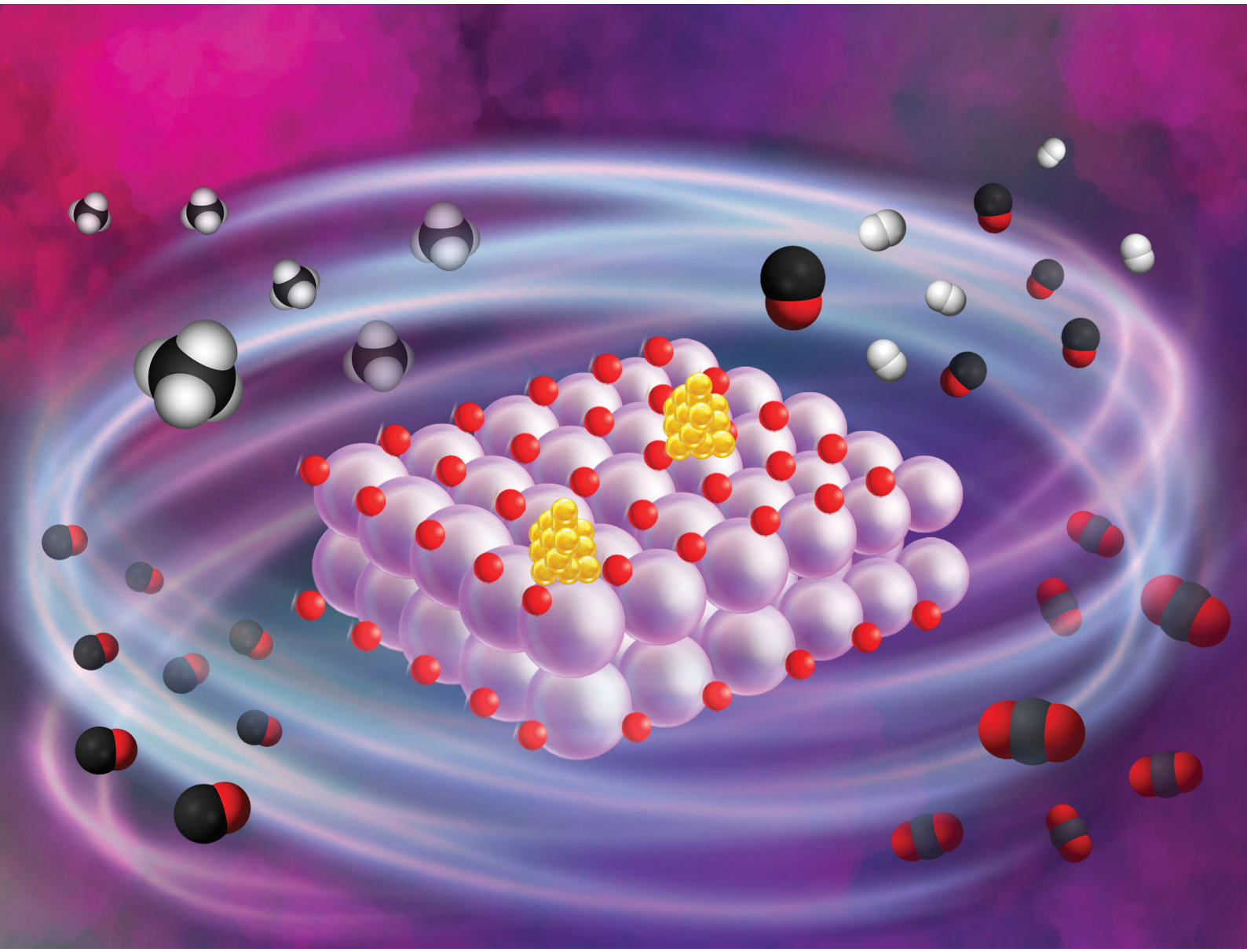

ISSN 2633-5409

ROYAL SOCIETY OF CHEMISTRY

PAPER

J. M. Serra *et al.*

Boosting methane partial oxidation on ceria through exsolution of robust Ru nanoparticles

Materials Advances

ROYAL SOCIETY OF CHEMISTRY

PAPER

View Article Online
View Journal | View Issue

Cite this: *Mater. Adv.*, 2021, 2, 2924

Boosting methane partial oxidation on ceria through exsolution of robust Ru nanoparticles†

A. J. Carrillo, L. Navarrete, M. Laqdiem, M. Balaguer and J. M. Serra *

Finding sustainable routes for the transformation of CO_2 into fuels and added-value chemicals is key for mitigating greenhouse gas emission. In this respect, chemical-looping reforming coupled with CO_2 splitting emerges as a promising technology to produce syngas, using waste or solar heat as an energy source. It relies on metal oxides that act as redox intermediates and, thus, the stability and catalytic activity of the oxides are crucial. For that purpose, ceria has been widely used due to its superior multicyclic stability and fast CO_2 splitting kinetics. However, it also presents low capacity for oxygen exchange or supply compared with other oxides and slow methane partial oxidation kinetics, which is normally improved by cationic doping or catalytic surface activation *via* metal impregnation. The high temperatures (900 °C) required for these reactions lead to catalyst deactivation over time due to sintering of metallic clusters. In order to circumvent this issue, in this work we have utilized the exsolution method to create uniformly dispersed Ru nanoparticles (*ca.* 5 nm) that remain anchored to the cerium oxide backbone, guaranteeing its microstructural stability and catalytic activity over prolonged cycling. We provide evidence for metallic Ru exsolution and further demonstrate the outstanding benefits of exsolved nanoparticles in the partial oxidation of methane following a chemical-loop reforming scheme, especially in the temperature range in which industrial waste heat could be used as an energy source to drive the reaction. Remarkably, at 700 °C surface functionalization with exsolved Ru nanoparticles enables high CO selectivity (99% *versus* 62% for CeO_2) and about 2 orders of magnitude faster H_2 production rates. The dispersion and size of the exsolved Ru nanoparticles were maintained after a durability test of 20 chemical loops at 900 °C, indicating their robustness. Overall, the results presented here point towards the unique characteristics of nanoparticle exsolution for preventing agglomeration, which could find application in other catalytic or electrochemical processes for target hydrocarbon production.

Received 18th January 2021,
Accepted 23rd February 2021

DOI: 10.1039/d1ma00044f

rsc.li/materials-advances

1. Introduction

The intensification of chemical processes through the implementation of membrane reactors or chemical-looping schemes[1] is an attractive alternative for the sustainable production of fuels with reduced CO_2 footprint and increased exergy efficiency.[2,3] In particular, chemical-looping reforming of methane (*e.g.* natural gas or biogas) coupled with CO_2 splitting represents a unique niche for production of fuels utilizing two greenhouse gases as reagents.[4] In the first step, CH_4 is partially oxidized with the lattice oxygen of a metal oxide, CeO_2 in this case (eqn (1); Fig. 1). This reaction results in the production of H_2 and CO, known as syngas, in a 2 : 1 molar ratio, which is ideal for further processing into liquid fuels *via* the Fischer–Tropsch process. In the second step, the reduced metal oxide is reoxidized with CO_2, producing CO (eqn (2)). Importantly, the first step, which is an endothermic reaction occurring at high temperatures (800–1000 °C), could be driven with waste[5] or concentrated solar heat[6–8]

$$CH_4 + 1/\delta CeO_2 \rightarrow (CO + 2H_2) + 1/\delta CeO_{2-\delta} \quad (1)$$

$$CO_2 + 1/\delta CeO_{2-\delta} \rightarrow 1/\delta CeO_2 + CO \quad (2)$$

$$\text{Net reaction: } CH_4 + CO_2 \rightarrow 2CO + 2H_2 \quad (3)$$

This 2-step cyclic process presents several operational advantages. First, the main side reaction in thermocatalytic dry reforming, reverse water gas shift, is avoided. Secondly, carbon depositions caused by methane cracking in the first step could be transformed into CO during the second step by the Boudouard reaction.[9] To guarantee the feasibility of the

Instituto de Tecnología Química, Universitat Politècnica de València-Consejo Superior de Investigaciones Científicas, Avenida Los Naranjos s/n, 46022 Valencia, Spain. E-mail: jmserra@itq.upv.es

† Electronic supplementary information (ESI) available. See DOI: 10.1039/d1ma00044f

process, it is key to find stable redox materials that could withstand repeated high-temperature thermochemical cycling. In this respect, ceria has been widely studied due to its high structural stability at high temperatures and fast CO_2 splitting kinetics,[6,10] based on its performance tested in solar-driven reactors.[9,11–13] However, the limited oxygen-exchange capacity of ceria could hamper its further applicability. In order to overcome this problem, doping with other cations, such as Zr[14] or La,[5] has been employed in order to increase the reducibility of cerium oxides and, subsequently, the fuel yields obtained by H_2O and/or CO_2 splitting. Morphological modifications[15] or combinations in the form of composites with other metal oxides such as perovksites[16] or binary oxides[17,18] have been also successfully tested. Additionally, during the methane partial oxidation (MPO) step, most literature reports show syngas selectivity far from 100%,[6] which results from the combustion of CH_4 with readily available oxygen anions at the CeO_2 surface producing CO_2 and H_2O. In order to solve this problem, surface promotion with metallic nanoparticles is commonly used in chemical looping reforming.[2] In the case of CeO_2, noble metals such as Pt or Rh[19] or Ni in Ti-doped CeO_2[20] have been employed to suppress the formation of oxygenated molecules and increase H_2 and CO selectivity. In the latter case, Ni decorated Ti-doped CeO_2 resulted in CO selectivity (S_{CO}) values of *ca.* 80%.[20] These metallic catalysts are commonly incorporated in the oxide surface *via* impregnation methods; however, at the high temperatures needed to drive the reduction of the metal oxide with methane, metal nanoparticles can suffer sintering with neighboring particles, which affects its catalytic activity during prolonged operation.[21] In this sense, the exsolution method emerges as a promising alternative to obtain more durable metal nanoparticles with high catalytic activity. Nanoparticle exsolution consists of migration, under reductive atmospheres, of metal cations contained in the oxide lattice to the oxide surface, forming nanoparticles that remain anchored to the oxide backbone.[22] The fact that the nanoparticles are socketed into the oxide surface imparts beneficial effects in terms of stability, avoiding nanoparticle sintering.[23] For this reason, exsolution has gained considerable attention in the field of solid oxide fuel cells and electrolyzers,[24,25] and more recently its application has been found to be promising in methane reforming reactions.[26–29] For instance, Kousi and co-workers obtained exsolved and submerged Ni nanoparticles on $La_{0.8}Ce_{0.1}Ni_{0.4}Ti_{0.6}O_3$ which synergistically enhanced the oxygen supply capacity.[26] Additionally, Co incorporation into the B-site enables the activation of methane at temperatures as low as 450 °C.[30] For simultaneous methane partial oxidation coupled with CO_2 splitting, Dimitrakopoulos *et al.* used a membrane reactor in which the exsolved nanoparticles were formed *in situ* during the reaction.[31] More recently, Carrillo *et al.* demonstrated the beneficial effects of Co exsolution in the $La_{0.6}Sr_{0.4}Cr_{0.8}Co_{0.2}O_3$ perovskite for syngas production, leading to faster MPO and CO_2 splitting rates, higher syngas selectivity and stable nanoparticle size over 28 chemical loops.[32] Regarding ceria and other fluorite type structures, the exsolution method has been scarcely explored. Recently, Naeem *et al.* demonstrated that Ru exsolution could boost the catalytic stability of $Sm_2Ru_xCe_{2-x}O_7$ materials for methane dry reforming, especially when compared with Sm–Ce pyrochlores with impregnated Ru particles, denoting the beneficial effects of nanoparticle anchoring *via* exsolution.[27] Based on these recent discoveries, in this work, we have applied the exsolution method to create robust Ru nanoparticles that could boost syngas production *via* chemical looping reforming of methane coupled with CO_2 splitting, which to date has not been tested for ceria-based materials. The results reported herein denote the benefits of nanoparticle exsolution and could open the path for designing more stable cerium catalysts for other thermocatalytic applications or solid oxide electrochemical reactors and electrolyzers.[33–36]

2. Results and discussion

2.1. Physicochemical insights into Ru nanoparticle exsolution on CeO_2

Ruthenium doped cerium oxide, $Ru_{0.01}Ce_{0.99}O_2$ (Ru–CeO_2), was prepared *via* a modified version of the Pechini method (see the Experimental section). For benchmarking, CeO_2 was also synthesized following the same method. According to the X-ray diffractograms depicted in Fig. 1, pristine Ru–CeO_2 and CeO_2 presented solely the reflections of fluorite CeO_2, space group *Fm*3*m*. Interestingly, incorporation of Ru into the fluorite crystal induced a lattice expansion according to the shift of the main reflection to lower 2θ values, pointing to the presence of a solid solution. The cubic lattice parameter, *a*, was calculated for both materials and was found to be 5.405 and 5.421 Å for CeO_2 and Ru–CeO_2, respectively. This result is somehow counter-intuitive since the ionic radius for Ce^{4+} in 8-fold coordination is

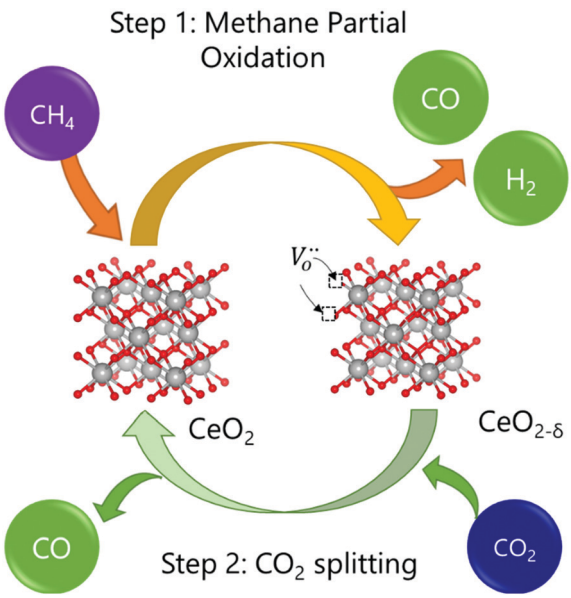

Fig. 1 Schematic of the chemical looping reforming of methane process studied in this work. In the first step, CH_4 reacts with the lattice oxygen from CeO_2, resulting in the formation of CO and H_2. In the second step, CO_2 reacts with the reduced oxide ($CeO_{2-\delta}$), replenishing the oxygen vacancies formed in the first step, and, subsequently, forming CO.

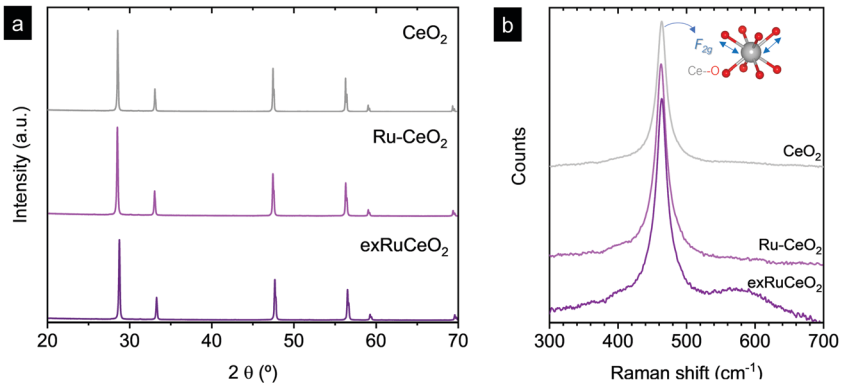

Fig. 2 X-ray diffraction patterns (a) and Raman spectra (b) for Ru–CeO_2 before and after exsolution performed at 900 °C for 2 h under 5% H_2 flow (exRuCeO_2) and for CeO_2. Raman spectra were collected with a 785 cm^{-1} laser. The inner sketch in (b) depicts the vibration of oxygen anions around the Ce cation associated with the F_{2g} Raman mode.

0.97 Å, whereas for Ru^{4+} (in 6-fold coordination) it is 0.64 Å,[37] which would suggest lattice shrinkage. However, this result is in accordance with previous works that reported a lattice expansion with Ru doping.[38,39] In order to confirm the lattice expansion upon Ru substitution we analyzed the materials with Raman spectroscopy (Fig. 2b). Due to the high symmetry of the cubic fluorite structure, CeO_2 has a unique Raman band ascribed to a one triply degenerate oxygen breathing mode of F_{2g} symmetry.[40] This mode normally occurs at 465 cm^{-1}; however, under the instrumental conditions used here, a red laser of 785 cm^{-1} wavelength, the F_{2g} peak for undoped CeO_2 is at 463.7 cm^{-1}. Upon Ru incorporation, the mode slightly shifted towards lower wavenumbers, 463.3 cm^{-1}, which corroborates the lattice expansion observed by XRD. Interestingly, no bands associated with oxygen vacancies, the region between 550 and 600 cm^{-1},[27] were observed for Ru–CeO_2.

Fig. 2a also shows the XRD diffraction patterns for Ru–CeO_2 material after the exsolution process performed at 900 °C for 2 h under a 5% H_2 atmosphere, revealing that the fluorite crystal phase prevailed after the reductive treatment without the appearance of any secondary phase. However, when scrutinizing the materials' morphology before and after exsolution, important differences were observed. Fig. 3 depicts the SEM images of Ru–CeO_2 before and after the exsolution treatment. Fig. 3a reveals that Ru–CeO_2 is formed by aggregates of necked micron-sized particles. Fig. S1 (ESI†) shows the EDX elemental analysis of the pristine material. However, after 2 h reduction in 5% H_2, well-dispersed nanoparticles emerged over the oxide surface indicative of nanoparticle exsolution (Fig. 3b). Turning back to the XRD diffraction, the exsolution treated Ru–CeO_2 sample (exRuCeO_2) experienced a shift towards higher 2θ values, denoting lattice shrinkage. That is to say, exRuCeO_2 presented a cubic lattice parameter, a, of 5.413 Å, whereas for the pristine sample it was 5.421 Å. This slight lattice contraction was also observed in the Raman spectra depicted in Fig. 2b. The F_{2g} peak position for exRuCeO_2 is at 464.5 cm^{-1}, which is one wavenumber higher compared to that for Ru–CeO_2. In addition, exRuCeO_2 exhibited the Raman modes ascribed to oxygen vacancies at around 550–600 cm^{-1}.[41] This indicates that the

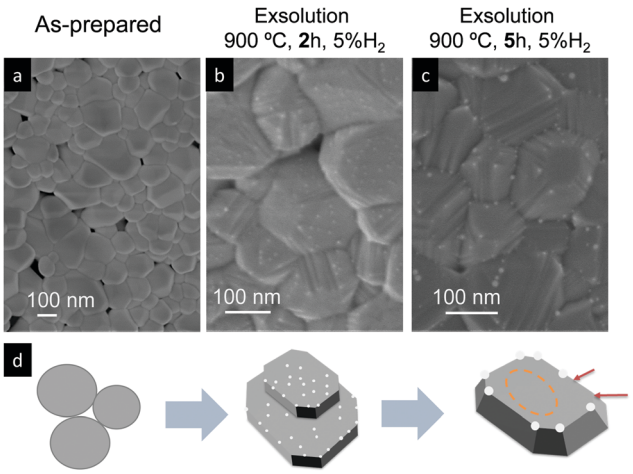

Fig. 3 SEM images of Ru-doped CeO_2 samples: (a) pristine and after exsolution treatment for (b) 2 h and (c) 5 h at 900 °C under a 5% H_2 atmosphere. (d) Schematic depicting the morphology transformations at each stage.

exsolution treatment in the reductive atmosphere triggers the creation of oxygen vacancies in addition to the exsolved nanoparticles. Although both XRD and Raman analyses point toward lattice contraction upon nanoparticle exsolution, the origin of this phenomenon is not clear. Previous reports on reduction of Ru–CeO_2 at 500 °C in a H_2 atmosphere showed a slight lattice expansion upon reduction;[38] however, in that work the presence of exsolved Ru nanoparticles was not inferred. Under the present reductive atmosphere, the lattice oxygen reacts with H_2 giving rise to electrons and oxygen vacancies, as demonstrated by Raman (Fig. 2b), which in the Kroger–Vink notation can be written as

$$H_2(g) + O_O^X \rightarrow V_O^{\bullet\bullet} + 2e^- + H_2O(g) \quad (4)$$

Subsequently, the oxidation state of cerium cations will be lowered according to $Ce^{4+} + e^- \rightarrow Ce^{3+}$.[42] Commonly, it has

been believed that lattice expansion of CeO_2 upon reduction has been ascribed to the larger ionic radii of Ce^{3+} (1.143 Å) compared to that of Ce^{4+} (0.97 Å) cations. However, Muhich demonstrated that Ce^{3+}–O^{2-} elongation can be compensated by Ce^{4+}–O contraction, with the lattice expansion being driven by non-counterpoised forces.[43] Anyhow, the nucleation of exsolved metallic nanoparticles compensates to a certain extent the expansion with contraction,[42] which for this particular case, $Ru^{4+} + 4e^- \rightarrow Ru^0$, could be higher explaining the slight lattice contraction upon metallic exsolution. In order to shed more light on this matter, we analyzed these three materials with Temperature Programmed Reduction (TPR). The TPR results (Fig. S2, ESI†) showed a common peak at *ca.* 800 °C peak maximum, ascribed to the reduction of the Ce^{4+} bulk species.[44] Interestingly, for both CeO_2 and $RuCeO_2$ this peak is located at 800 °C. Normally, partial substitution of Ce^{4+} in doped ceria materials leads to a shift of this peak toward lower temperatures due to the creation of oxygen vacancies that facilitate oxygen diffusion.[45,46] However, in this case Ru-doping did not result in the same effect, which might corroborate that Ru cations are located in interstitial positions, rather than partially substituting the Ce^{4+} cations, which results in the lattice expansion. After the exsolution treatment (5% H_2, 900 °C, 2 h) of the $exRuCeO_2$ material, the main peak shifted to 769 °C. This shift to lower temperatures is ascribed to the presence of oxygen vacancies, as corroborated by Raman spectra. This fact is in principle beneficial for the MPO step, indicating that $exRuCeO_2$ could outperform CeO_2 at lower temperatures. Additionally, with the TPR analyses it was possible to determine the oxygen exchange/supply capacity of the materials (see the Experimental section for more details). Our results indicate that the oxygen supply capacity of $exRuCeO_2$ was equal to 0.18 mol O mol_{oxide}^{-1}, whereas for CeO_2 it was 0.09 mol O mol_{oxide}^{-1}. Despite the increased value for $exRuCeO_2$ with respect to CeO_2, the oxygen supply capacity is still below the values reported for perovskites, for instance *ca.* 0.4 mol O mol_{oxide}^{-1} for $La_{0.8}Ce_{0.1}Ni_{0.4}Ti_{0.6}O_{3-\delta}$.[30]

SEM analysis (Fig. 3b) of the sample reduced for 2 h in H_2 at 900 °C reveals the formation of exsolved nanoparticles ($d \sim 2$–5 nm), well dispersed over all the facets of the oxide. Interestingly, when increasing the exsolution treatment up to 5 h (Fig. 3c) the nanoparticle size increases, as previously observed in Ni exsolution in perovskites,[47,48] and grow mainly in the edges of the oxide particles, which progressively change from a rounded-like shape into a more faceted morphology caused by a longer exposure to the reductive environment. The changes in the exsolved nanoparticle habitus depending on time are reflected in the schematic depicted in Fig. 3d.

We now turn to TEM to further analyze the size and level of anchorage of the exsolved Ru nanoparticles. Fig. 4a depicts some grains of $exRuCeO_2$ and the presence of exsolved nanoparticles over the oxide backbone. At higher magnifications (Fig. 4b), it is possible to observe that the nanoparticle is embedded in the oxide backbone, confirming the level of anchorage characteristic from metal nanoparticle exsolution.[49] Fig. 4c shows the HAADF-STEM image of $exRuCeO_2$, in which it

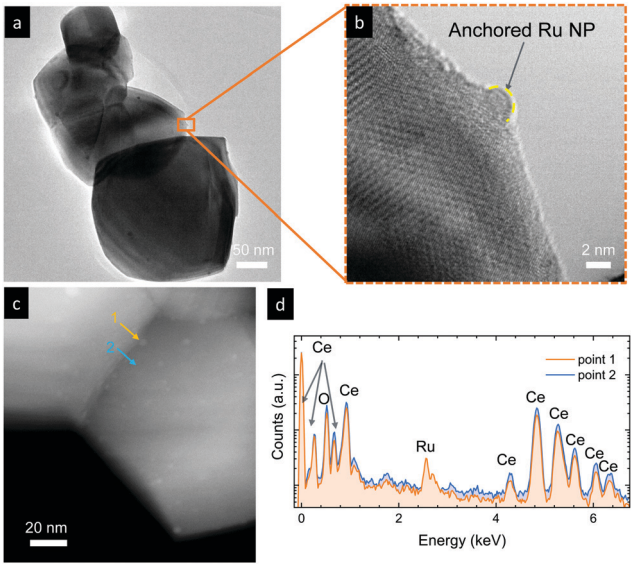

Fig. 4 (a and b) TEM images of Ru-doped CeO_2 after exsolution treatment for (b) 2 h at 900 °C in a 5% H_2 atmosphere. (c) HAADF-STEM image for the same material and (d) EDX point analysis of an exsolved nanoparticle (point 1) and the bare oxide surface (point 2).

is possible to observe the high and uniform dispersion of exsolved nanoparticles over the oxide backbone. EDX was utilized to further explore the nature of the exsolved nanoparticles (Fig. 4d), by analyzing two different zones in Fig. 4c, one pointing to an exsolved particle (point 1) and the other pointing to the oxide surface (point 2). By comparison, one can observe the higher concentration of Ru on the exsolved nanoparticles. Although Ru exsolution on $Sm_2Ce_2O_7$ pyrochlores has been recently reported,[27] to the best of our knowledge this work represents the first demonstration of Ru exsolution from the CeO_2 fluorite host.

To further explore the nature of the exsolved nanoparticles we performed X-ray photoemission spectroscopy (XPS; Fig. 5). In order to analyze the oxidation state of Ru, we checked the Ru3p core shell, since Ru5d overlaps with C1s.[34,38,39] Fig. 5a compares the Ru3p spectra for Ru–CeO_2 before and after exsolution (*i.e.*, for $exRuCeO_2$). The $Ru3p_{3/2}$[50] binding energy for Ru–CeO_2 was observed at 463.26 eV, whereas after exsolution, it shifted to 461.64 eV, indicative of the Ru metal.[34,38,39] This shift indicates that for the Ru–CeO_2 sample Ru is in the 4+ oxidation state, and after the 2 h reduction in 5% H_2 at 900 °C, all the Ru at the surface is in the metal state, corroborating that the exsolved nanoparticles observed by SEM (Fig. 3) and TEM (Fig. 4) are solely composed of the Ru metal. XPS analysis of Ce3d core-level spectra are depicted in Fig. 5b. The $3d_{5/2}$ and $3d_{3/2}$ components correspond to v and u, respectively, whereas v″, v‴ and u″, u‴ are the satellites, respectively. Additionally, the doublets v_0, u_0 and v′, u′ correspond to Ce^{3+}.[51–53] A detailed description of the deconvolution of each of these components can be found in the ESI† (Tables S1–S3,). According to the spectra depicted in Fig. 5b, it can be inferred that there is little presence of Ce^{3+} in the surface of Ru–CeO_2, which slightly increases after exsolution, as revealed for $exRuCeO_2$. The O1s spectra depicted in Fig. 5c indicate that for the three materials the major component is

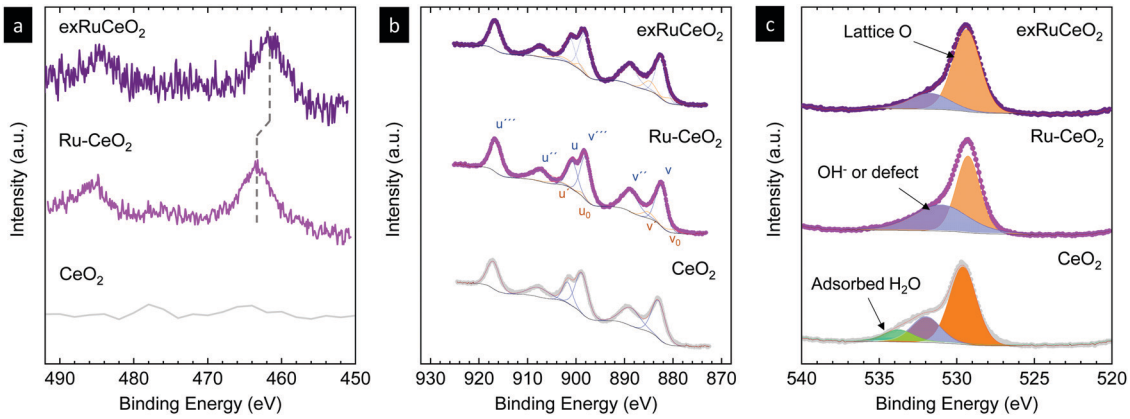

Fig. 5 X-ray photoemission spectra of (a) Ru3p, (b) Ce3d and (c) O1s core levels of CeO_2 and Ru-doped CeO_2 before (Ru–CeO_2) and after exsolution of Ru nanoparticles (exRuCeO$_2$).

located at binding energies around 529 eV, which is generally ascribed to the lattice oxygen in oxides.[51] In addition, for Ru–CeO_2 and exRuCeO$_2$ there is a feature around 531 eV representative of oxygen anions in the vicinity of oxygen vacancies, indicating the presence of oxygen vacancy sites in the surface of these materials. For the case of CeO_2, the components around 533 and 534 eV could be ascribed to adsorbed species.

In this section, we have presented the thorough physico-chemical characterization of the materials before and after exsolution, confirming the presence of anchored metallic Ru nanoparticles over cerium-based oxides. In the following, the performance of exRuCeO$_2$ for chemical looping methane reforming coupled with CO_2 splitting will be interrogated, paying special attention to the reaction rate improvement and nanoparticle stability after prolonged cycling.

2.2. Improving methane partial oxidation with Ru exsolution

Chemical looping methane reforming coupled with CO_2 splitting reactions was performed in a fixed-bed tubular quartz reactor and the gas production was monitored *via* mass spectrometry. First, we focus on determining the impact of Ru nanoparticles on syngas production, and for that, we benchmark exRuCeO$_2$ against CeO_2. As commented in the introduction, one of the main drawbacks of CeO_2 for chemical looping reforming is that it presents slow syngas production during the partial oxidation of methane, which is the first step of this redox cyclic process (Fig. 1). In this first set of experiments, chemical looping reforming coupled with CO_2 splitting was assessed at three different temperatures (900, 800, 700 °C) for both materials, *i.e.*, exRuCeO$_2$ and CeO_2. Here, it should be noted that the exsolution process was carried out inside the reactor, prior to the chemical looping reforming tests. We first assessed the influence of temperature on the chemical looping reforming performance of CeO_2. Fig. 6a depicts the reactions occurring at 900 °C, which start with the injection of a stream of 5 vol% of CH_4, resulting in the formation of H_2 and CO, which are the products of the partial oxidation of methane, and CO_2, which results from the complete oxidation of CH_4 with the lattice oxygen. For further information, Fig. S3 (ESI†) also shows the CH_4 curve in order to show the methane consumption, as well as the O_2 production curve, which clearly illustrates the absence of this gas during the experiments. The formation of CO_2 occurred at the beginning of the reaction, which is indicative of CH_4 reaction with readily available oxygen species at the surface of the ceria.[54] The CO_2 production in the first stage of the reaction lasted for *ca.* 1 min. Simultaneously, the formation of H_2 and CO occurred steadily until CH_4 injection was suppressed. At 900 °C, CO selectivity, S_{CO}, was equal to 80% because of the prominent formation of CO_2; see Fig. 7 for the selectivity data at the different temperatures tested. The peak gas production rate was 2.9 and 1.3 mL min^{-1} g^{-1} for H_2 and CO, respectively, resulting in a H_2:CO ratio slightly higher than the stoichiometric 2:1 proportion, indicative of CH_4 decomposition into solid C and additional H_2 formation. Once CH_4 injection was complete, Ar was flushed to purge the reactor for 2 min, followed by the injection of CO_2 (5 vol%). As mentioned in the introduction (Fig. 1), the methane partial oxidation step generates oxygen vacancies in the cerium oxide, since the lattice oxygen reacts with CH_4. Thus, in the oxidation step, CO_2 reacts with the reduced cerium oxide ($CeO_{2-\delta}$), replenishing most of the oxygen vacancies with oxide anions, and subsequently forming CO, as observed in the second step in Fig. 6a. Once CO_2 is injected inside the reactor, a fast CO production is observed (peak production rate of 18.2 mL min^{-1} g^{-1}), that lasted for 2 min until CO_2 splitting reaction reached equilibrium. This fact indicates that this $CeO_{2-\delta}$-reoxidation step could be performed with shorter CO_2 injections, which will eventually increase the CO_2 conversion per cycle, denoting the high extent of operational tunability and room for optimization of this technology.

The influence of temperature on the chemical looping reforming activity of CeO_2 is depicted in Fig. 6b (reaction at 800 °C) and Fig. 6c (reaction at 700 °C). Here, we would like to note that lowering the process temperature is beneficial to leverage industrial waste heat to drive the endothermic methane partial oxidation reaction.[5] However, by lowering the reaction temperature, the driving force for the formation of oxygen vacancies in CeO_2 and the activation of CH_4 are also decreased since, thermodynamically, oxygen vacancy formation

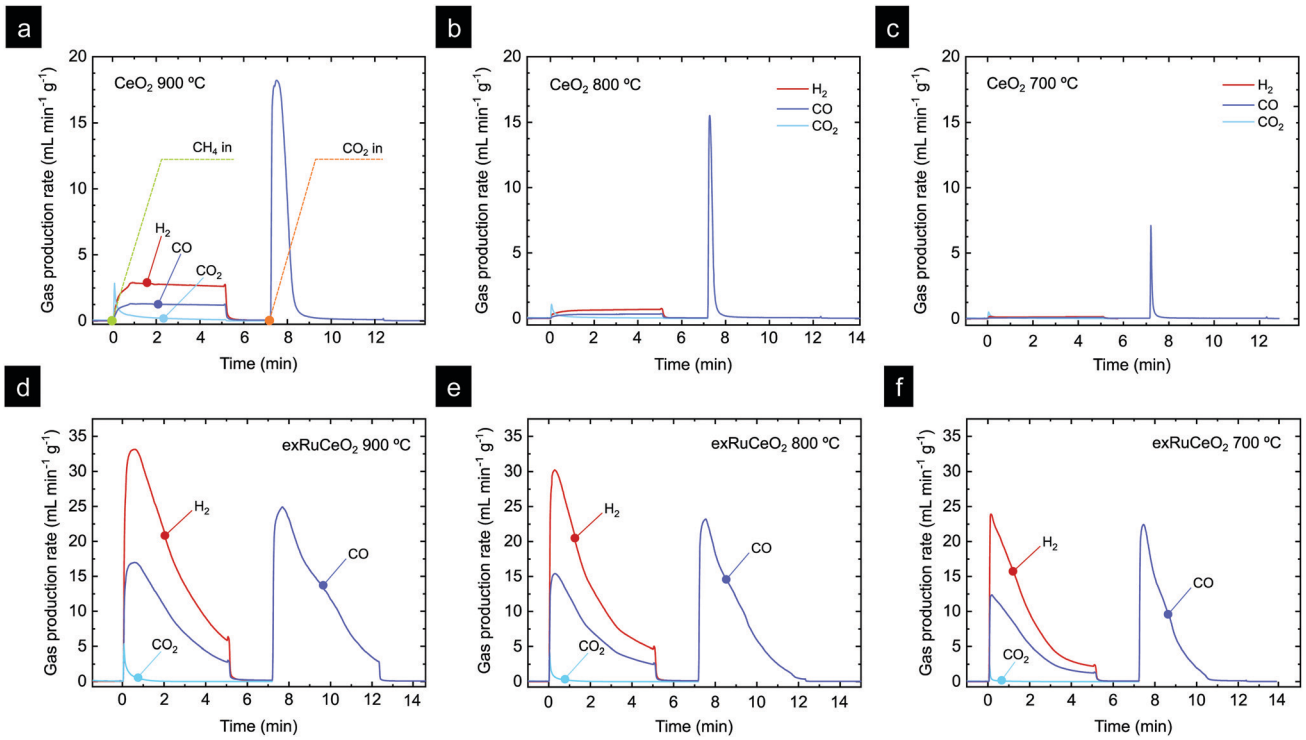

Fig. 6 Chemical looping gas production curves for CeO_2 at (a) 900 °C, (b) 800 °C and (c) 700 °C, and $exRuCeO_2$ at (d) 900 °C, (e) 800 °C and (f) 700 °C. Each chemical loop consisted of 5 min methane partial oxidation (injection of 5% CH_4, total flow 100 mL min^{-1}) and 5 min CO_2 splitting (injection of 5% CO_2, total flow 100 mL min^{-1}). The exsolution of $exRuCeO_2$ was performed inside a quartz reactor. For that purpose, Ru–CeO_2 was reduced under 5% H_2 for 2 h at 900 °C.

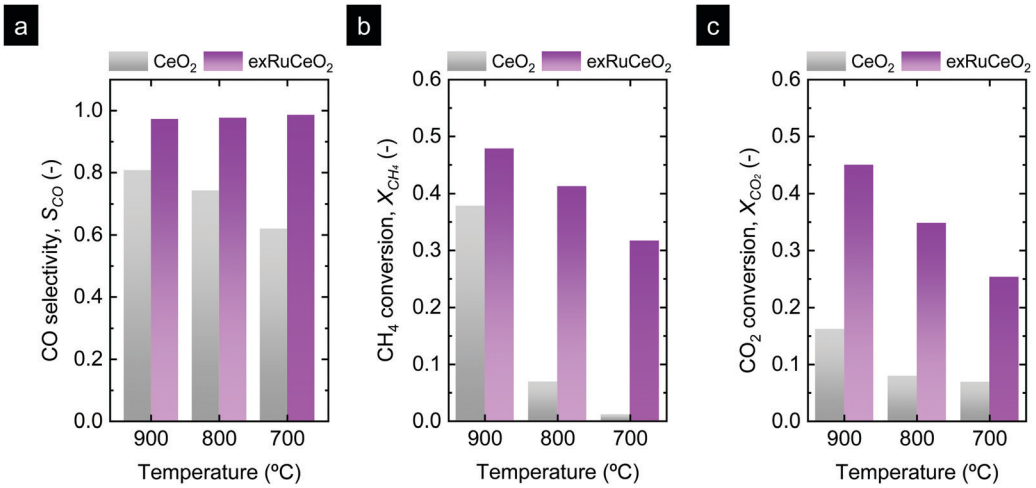

Fig. 7 Comparison of (a) selectivity, (b) CH_4 conversion during the MPO step, and (c) CO_2 conversion during the CO_2 splitting step for the two materials tested.

in ceria is favored at higher temperatures.[54] This fact implies that lower reduction extents, δ, are achieved during the methane partial oxidation, which directly affects the CO production extent (yield and formation rate) in the subsequent CO_2 splitting step (eqn (1) and (2)). This effect is illustrated in Fig. 6b and c, *i.e.* lowering the reaction temperature drastically diminished the amount of H_2 and CO produced in the first step, and hence the CH_4 conversion, with peak H_2 production rates of 0.76 and 0.18 mL min^{-1} g^{-1}, denoting one order of magnitude decrease in the syngas production of CeO_2 by lowering 200 °C. This temperature decrease also affected S_{CO}, which decreased to 74% and 62% at 800 and 700 °C, respectively. Fig. S4 (ESI†) (a zoom-out of Fig. 6c) reveals that the CO_2 production curve is even higher than the H_2 and CO ones. In addition, the CO_2 splitting rate and CO yield notably decreased at lower temperatures, as an effect of the lower amount of

vacancies created in the methane activation step, which directly correlates with the amount of CO produced in the second step. The CO yields obtained were 14.1, 3.5 and 0.5 mL g^{-1} for 900, 800 and 700 °C, respectively. In addition, for the reaction at 900 °C, there is a fraction of CO that was generated through the Boudouard reaction, in which deposited coke is gasified with CO_2, increasing CO yield. In summary, these results provide evidence about the main challenges of CeO_2 in chemical looping reforming, *i.e.* (i) low activity for methane partial oxidation; and (ii) syngas selectivity far from 100%, both being drastically decreased with lowering the process temperature.

Fig. 6d–f show the results of catalytic tests using exRuCeO$_2$ as a redox material at 900, 800 and 700 °C, respectively. By comparing Fig. 6a and d, the benefits of surface functionalization by exsolved Ru nanoparticles become noticeable. At 900 °C the H_2 production rate for exRuCeO$_2$ is 33.1 mL min^{-1} g^{-1} with a H_2 production of 92 mL g^{-1}. In contrast, the values achieved for CeO_2 are 2.9 mL min^{-1} g^{-1} and 13.70 mL g^{-1}, which are *ca.* one order of magnitude lower. In addition, the gas production curve when using exRuCeO$_2$ starts with a pronounced peak that progressively decays, which totally differs from the flattened profile exhibited for syngas production with CeO_2. The amount of CO produced is 46.6 mL g^{-1}, resulting in a H_2 : CO ratio of 1.98 close to the stoichiometric 2 : 1. In comparison CeO_2 showed a H_2 : CO ratio of 2.17 at 900 °C, due to CH_4 cracking into H_2(g) and C(s). This is indicative of a higher resistance to carbon depositions ascribed to the presence of exsolved nanoparticles, as previously reported in the literature.[23] Fig. 6a also shows that there is concomitant production of CO_2, however, in a minor extent when compared with CO, resulting in a high S_{CO} of 97%. These results highlight the benefits that exsolved Ru nanoparticles impart on improving the methane partial oxidation performance. However, it should be also kept in mind that exRuCeO$_2$ allocates oxygen vacancies prior to the reaction since during the exsolution treatment H_2 was utilized to reduce the material and drive the exsolution of Ru nanoparticles. Warren and Scheffe pointed towards surface oxygen vacancies as active sites for methane activation,[55] and recently demonstrated how the increase of oxygen vacancies in CeO_2, in their case by not reaching full conversion in the previous CO_2 splitting oxidation step, could greatly enhance the rate of syngas production.[9]

The higher syngas yield in the first step is an indicative of a higher extent of reduction for exRuCeO$_2$ when compared with CeO_2, triggered by the presence of Ru. As a result, in the subsequent CO_2 splitting step, the CO yield (Fig. 6d) was also higher than for CeO_2 (Fig. 6a) with 14.1 and 66 mL g^{-1}, respectively. It can be also observed that for exRuCeO$_2$, the CO_2 splitting reaction did not achieve equilibrium in the 5 min CO_2 injection, opposite to the behavior of CeO_2, which reached full oxidation after 2 min exposure.

Similar to what happened to CeO_2, lowering the temperature also affected the kinetics and syngas yield, although to a minor extent (Fig. 6e and f). In particular, the performance observed at 700 °C is remarkable (Fig. 6f), which is the temperature closer to the range needed for utilization of industrial waste heat as an energy source. For instance, the peak H_2 production rate reaches 23.9 mL min^{-1} g^{-1} for exRuCeO$_2$, whereas for CeO_2 it is 0.18 mL min^{-1} g^{-1}. This 2-order of magnitude increase in the syngas production rate at 700 °C illustrates the high catalytic activity of the Ru nanoparticles for the MPO into syngas. In addition, exRuCeO$_2$ displayed S_{CO} ~ 99% at 700 °C. Fig. 7b shows that methane conversions (X_{CH4}) ~ 32% can be reached for exRuCeO$_2$ at 700 °C whereas for CeO_2 just 1% conversions are observed. Nevertheless, it should be noted here that our experiments were not targeted for reaching higher conversions of CH_4 or CO_2, which could be improved by shortening the injection time or increasing the solid loading. For the CO_2 splitting step, just a slight decrease is observed in the peak production rate when lowering the temperature. That is to say, CO production rates were 24.9, 23.2 and 22.4 mL min^{-1} g^{-1} at 900, 800 and 700 °C, respectively. However, since by lowering the temperature the amount of oxygen vacancies generated in the previous reduction step was also decreased, it was observed that CO_2 splitting reaction reached equilibrium before the 5 min CO_2 injection was complete. That is to say, at 700 °C, CO_2 splitting reached equilibrium after 3 min of exposure to CO_2 (Fig. 6f) ascribed to a lower amount of oxygen vacancies that should be replenished. This also affected the CO_2 conversion values (X_{CO2}) which increased with increasing temperature (Fig. 7c). The highest conversion was for exRuCeO$_2$ at 900 °C with *ca.* 45%, whereas for CeO_2 it was *ca.* 16% at the same temperature.

2.3. Chemical activity and stability test of exsolved Ru nanoparticles

In the previous section, the benefits of functionalizing the CeO_2 oxide surface with Ru nanoparticles became visible, with a remarkable reaction activity improvement when compared with bare CeO_2. Now, we assess the stability of the reaction over prolonged cycling at a fixed temperature as well as the stability of the Ru nanoparticles in harsher conditions. For that purpose, we conducted a 20-cycle chemical looping reforming test at 900 °C. The reaction conditions were modified with respect to the previous section, *viz.*, a 10-fold higher concentration of CO_2 (50 vol%) was used for the 2nd step. The motivation for the increase of the CO_2 partial pressure was 2-fold. The first was in order to assess the reaction in more realistic conditions in which more concentrated CO_2 stream would be used. Second, we observed in Fig. 6d that with 5 vol% the CO_2 splitting reaction did not reach equilibrium in the given 5 min CO_2 injection period. By increasing the CO_2 partial pressure faster kinetics are expected,[56] achieving full oxidation in the given time. By this way, the material will be fully oxidized in the subsequent reduction step under CH_4, and, thus, the kinetic effect provided by the oxygen vacancies acting as active sites at the surface will be suppressed. Raman (Fig. 2b) and XPS analyses (Fig. 5c) proved that exRuCeO$_2$ allocates oxygen vacancies before the first MPO reaction, which Warren and Scheffe showed to be vacancy-mediated.[55] The syngas production curves during the 20-cycle chemical looping reforming test are shown in Fig. 8a, in which the syngas (H_2 and CO) produced during the MPO and the CO produced during the CO_2 splitting step are depicted. It can be observed that over the 20 cycles, the chemical activity of the

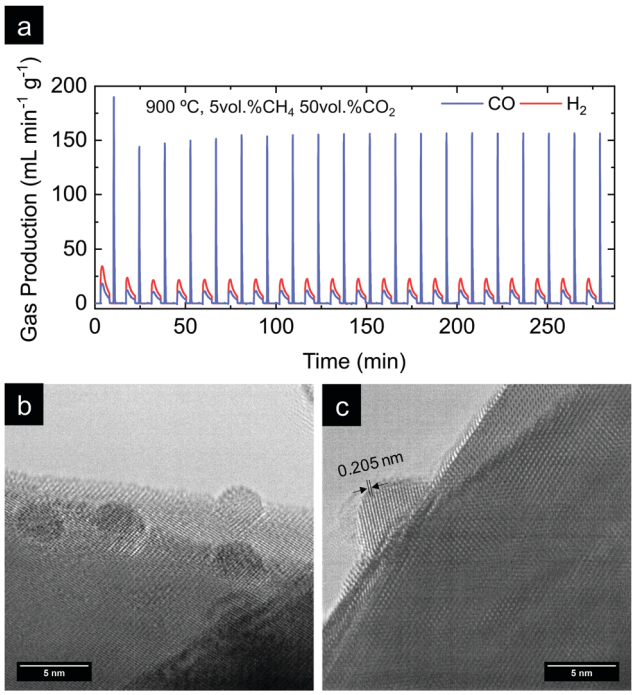

Fig. 8 (a) H_2 and CO gas production curves obtained from a durability test carried out for $exRuCeO_2$, previously exsolved in a tubular furnace at 900 °C for 2 h under 5% H_2. The test consisted of 20 chemical loops, with each of them with first 5 vol% CH_4 injection for 5 min, followed by a 2 min purge under pure Ar, and 50 vol% CO_2 injection for 5 min. The total flow rate was always kept at 100 ml min^{-1}. (b and c) TEM images of $exRuCeO_2$ after the 20 chemical loops of methane reforming coupled with CO_2 splitting, illustrating the stability of the exsolved Ru nanoparticles. In (c) the interplanar distance of the exsolved particle after 20 cycles is illustrated.

$exRuCeO_2$ material is preserved, although some differences with respect to the chemical looping test in Fig. 6d are visible. First, regarding the CO production during the CO_2 splitting step; with the increase in the vol% of CO_2, the peak production rate is greatly enhanced. That is to say, in Fig. 6d we observe a peak production rate of 24.9 mL min^{-1} g^{-1} when using 5 vol% of CO_2, whereas when increasing the concentration up to 50 vol%, the rate increases up to 189. 9 mL min^{-1} g^{-1}, which is about a 7-fold increase. However, this high value was not maintained during the whole cycling test, and after a small decrease in the second cycle, it shows stable values at around 156 mL min^{-1} g^{-1} from the 6th to the 20th cycle. To put these results into perspective, Ruan *et al.* reported 168.8 mL min^{-1} g^{-1} using 100 vol% CO_2 and Ti-doped CeO_2 impregnated with metallic Ni.[20] In addition, on increasing the vol% of CO_2 the reaction reached equilibrium in *ca.* 1 min (see Fig. S5 in the ESI†). This fact indicates that complete equilibration in CO_2 *via* re-oxidation is achieved, and, thus, in the subsequent MPO step, the effect of additional oxygen vacancies – generated upon exsolution – as active sites for the activation of methane could be ruled out. Indeed, when comparing the syngas production curves between the first methane injection and the second, this effect becomes evident. That is to say, during the first MPO reaction, the H_2 production is 34.4 mL min^{-1} g^{-1}, which is very close to the reported value in Fig. 6a wherein the same conditions of 5 vol% of CH_4 and 900 °C were employed. However, in the second cycle the peak H_2 production rate lowers down to 23.4 mL min^{-1} g^{-1}, which is ascribed to the initial lack of surface oxygen vacancies that help in activating MPO. Thus, after the first cycle, since high CO_2 concentrations are used and, hence, full oxidation achieved, the catalytic improvement for the MPO could be solely ascribed to the exsolved Ru nanoparticles. Importantly, from the 2nd to the 20th cycle the MPO performance was stable (Fig. 8a) with a H_2 production rate around 23.4 mL min^{-1} g^{-1}.

Next, we assessed the microstructural stability of the exsolved Ru nanoparticles after the 20-cycle longevity test depicted in Fig. 8a. For that purpose, we analyzed with TEM the materials after reaction (Fig. 8b and c). In Fig. 8b, we provide evidence for the existence of Ru nanoparticles that remained well dispersed over the oxide surface after the multi-cycle treatment at high temperatures. Since the images were taken after the last CO_2 splitting step, this also proves that the exsolved Ru nanoparticles are not dissolved back into the lattice under these experimental conditions used in the oxidation step. This is probably due to the short exposure (5 min) to a less oxidative atmosphere (CO_2) when compared to air, which is the gas used in re-dissolution treatments. Thus, under these oxidative conditions there is not enough driving force to produce the dissolution of the exsolved

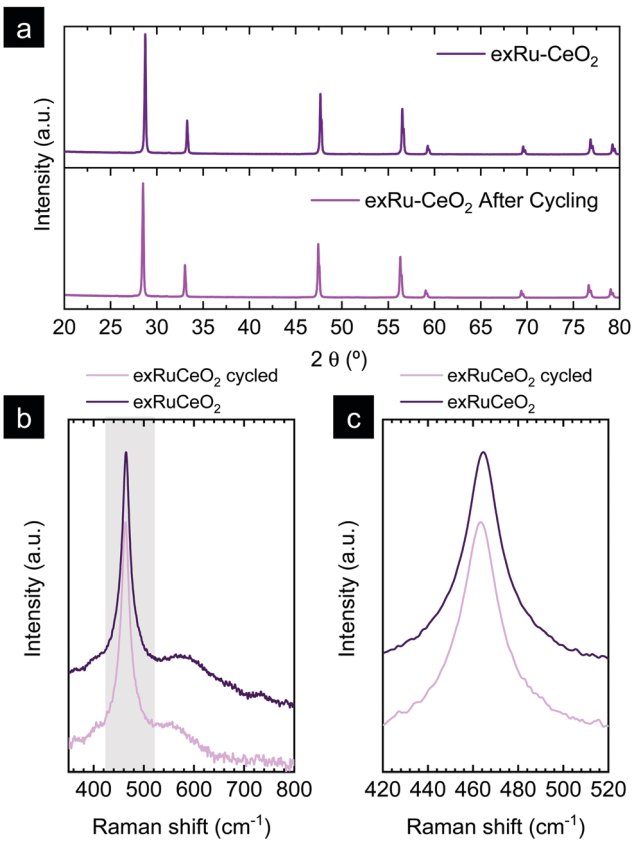

Fig. 9 (a) XRD diffractograms comparing $exRuCeO_2$ before and after the 20-cycle chemical looping reforming test. (b) Raman spectra comparison of $exRuCeO_2$ before and after 20 cycles. They grey-shaded region is zoomed out in (c) to show the shift of the F_{2g} peak towards lower Raman shift values. The Raman spectra were collected with a 785 cm^{-1} laser.

Ru nanoparticles back to the ceria backbone. This fact was previously reported with Co exsolution in $La_{0.6}Sr_{0.4}Cr_{0.8}Co_{0.2}O_3$ perovskites.[32] The nanoparticles of 4–5 nm remained well-dispersed and anchored to the oxide backbone, which prevented nanoparticle agglomeration. Fig. 8c provides further evidence of the level of anchoring. The interplanar distance of the exsolved nanoparticle was determined to be equal to 0.205 nm, which corresponds to the (101) orientation in metallic Ru, which further corroborates the nature of the exsolved nanoparticles.

The X-ray diffractogram of ex$RuCeO_2$ before and after the 20 chemical looping reforming cycles is depicted in Fig. 9a. After cycling, the material presented the peaks associated with the fluorite crystal structure. However, the calculated cubic lattice parameter was 5.422 Å, whereas before reaction it was 5.413 Å, indicating lattice expansion upon cycling, returning to lattice volume values similar to the material before exsolution (a = 5.421 Å for Ru–CeO_2). Raman spectroscopy was employed to further analyze the structural changes after multiple cycling (Fig. 9b and c). Fig. 9b reveals that after cycling the F_{2g} vibration is still the main component. However, as observed in the zoom-out area depicted in Fig. 9c, the F_{2g} shifted towards lower wavenumbers, with respect to the freshly exsolved material. That is to say, after 20 cycles the F_{2g} peak value moved to 463.1 cm^{-1}, whereas before reaction it was 464.5 cm^{-1}, displacement that confirms the lattice expansion observed by XRD analysis.

In summary, in this section we proved both the microstructural and chemical stability of the Ru nanoparticles over prolonged cycling at high temperatures, which remarks the key benefits of applying exsolution in high temperature thermocatalytic processes.

3. Conclusions

In this work, we have synthesized CeO_2 decorated with Ru nanoparticles of *ca.* 5 nm *via* the exsolution method and tested its activity for chemical looping reforming of methane coupled with CO_2 splitting, to address the main limitations that bare CeO_2 presents in this process. With TEM, EDX and XPS we provide proof of Ru nanoparticle exsolution and anchorage on CeO_2 for the first time, which were well dispersed all over the oxide surface. The chemical-looping reforming activity was tested and compared against reference – undoped – CeO_2, observing a remarkable increase in the syngas yield and production rate as well as carbon monoxide selectivity of 99% at 700 °C. Particularly remarkable is the syngas production result at such temperature, which matches perfectly operation utilizing industrial waste heat. That is to say, at 700 °C, a peak H_2 production rate of 23.9 mL min^{-1} g^{-1} was obtained for the material decorated with exsolved Ru nanoparticles, whereas for bare CeO_2 it was just 0.18 mL min^{-1} g^{-1}, which is two orders of magnitude less. Finally, the durability of the process was tested for 20 consecutive chemical loops denoting the remarkable stability of the morphology of exsolved nanoparticles after prolonged cycling. In summary, the findings presented here confirm the robustness of CeO_2-surface-anchored exsolved Ru nanoparticles as catalysts in high temperature thermochemical processes.

4. Experimental methods

4.1. Material synthesis

CeO_2 and $Ru_{0.01}Ce_{0.99}O_2$ (Ru–CeO_2) were synthesized by a modified version of the Pechini method. Cerium(III)nitrate ($Ce(NO_3)_3{\cdot}6H_2O$, 99%; Sigma Aldrich-Merck) and ruthenium(III)nitrosyl nitrate solution ($Ru(NO)(NO_3)_x(OH)_y$, $x + y = 3$, 1.5% Ru; Sigma Aldrich-Merck) were dissolved in an aqueous solution of citric acid (CA, 99%; Sigma Aldrich-Merck) at 60 °C under constant stirring for 3 h, using a metal precursor : CA molar ratio of 1 : 1.5. Afterward, ethylene glycol (EG, 99%; Sigma Aldrich-Merck) was added to the mixture to a CA : EG ratio of 2/3 wt% and the temperature was increased to 80 °C for 2 h. After most of the solution was evaporated, it was transferred to a drying oven and heated at 220 °C overnight, during which gelification and calcination of the gel took place. Then, the dry powder was ground into a fine powder using an agate mortar and calcined at 1000 °C for 10 h to obtain the fluorite phase. Nanoparticle exsolution on Ru–CeO_2 was performed in a horizontal tubular furnace at 900 °C, during 2 h under 5% H_2/Ar flow, unless otherwise specified in the text.

4.2. Physicochemical characterization

X-ray diffractometry (XRD) was performed utilizing a PANalytical CubiX fast diffractometer using CuKα1,2 radiation and a X'Celerator detector in Bragg–Brentano geometry. XRD patterns were recorded in the 2θ range 20° to 90° and analyzed using the software X'Pert Highscore Plus.

X-ray photoelectron spectra were collected by using a SPECS spectrometer equipped with a Phibos 150 MCD-9 detector and by using a non-monochromatic AlKa (1486.6 eV) X-ray source and charge compensation by means of additional electron flow. Spectra were recorded by using an analyzer pass energy of 50 eV and an X-ray power of 100 W under an operating pressure of 10^{-9} mbar. During data processing of the XPS spectra, the binding energy (BE) values were referenced to C1s (peak at BE = 248.8 eV). Spectra treatment was performed using CasaXPS processing software.

Raman spectroscopy was performed using a Renishaw Raman spectrometer. Analyses were conducted at room temperature with a 785 nm laser equipped with an Olympus microscope and a CCD detector.

The morphology of the synthesized oxides was analyzed *via* scanning electron microscopy (SEM) using a GeminiSEM 500 from Zeiss and transmission electron microscopy (TEM) using a JEM 2100F 200 kV field emission microscope equipped with a Gatan OneView camera. Energy dispersive X-ray spectroscopy elemental point scan analyses were conducted using EDS X-Max 80 de Oxford Instruments, with a 127 eV resolution.

The Micromeritics system was used to carry out temperature-programmed reduction (TPR). 100 mg of sample was pelletized and degassed under Ar flow for 1 h and then was subjected to reduction under H_2/Ar (1/9) flow, with a heating rate of 10 °C min^{-1} until 950 °C. H_2 consumption was measured by using a TCD.

4.3. Chemical looping reforming test

Chemical looping reforming of methane coupled with CO_2 splitting was carried out in a fixed-bed reactor setup. The

reactor consisted of a quartz tube of $\frac{1}{2}$ inch inner diameter placed inside a tubular vertical electrical furnace. The oxide samples (0.265 g) were placed over a quartz frit located at half of the quartz tube (total length 41 cm). The temperature was controlled with a K-type thermocouple in contact with the oxide bed and covered by a quartz shield. For the reaction tests, the materials were pressed into pellets, crushed and sieved for the size between 200 and 400 μm. The gas production was monitored using a Thermostar mass spectrometer from Pfeiffer, which was calibrated by flowing known gas concentrations before each reaction. In a typical experiment, the temperature was raised to 900 °C under an Ar (Praxair) atmosphere (100 mL min^{-1}). Then, the materials were pretreated under 5% H_2 balanced with Ar atmosphere for 2 h to drive the nanoparticle exsolution, unless otherwise specified. Afterward, each chemical loop consisted of 5 min injections of first, 5% CH_4, and second, 5% CO_2, both balanced in Ar. Between both injections, Ar was flowed to purge the reactor of reactive gases for 2 min. The gas bottles were of 10% CH_4 balanced in Ar and 15% CO_2 balanced in Ar.

For the longevity test consisting of 20 chemical loops, a thinner quartz tube was used with an internal diameter of 0.7 cm. In addition, for the oxidation step a stream of 50 vol% of CO_2 was used utilizing a 100% CO_2 gas bottle and a total gas flow of 100 mL min^{-1}.

CO_2 and CO m/z signal overlapping was corrected through the following equation according to Sastre *et al.*[57]

$$[CO] = S(m/z = 28) - f \cdot (m/z = 44) \quad (5)$$

where f is the ratio between m/z = 28 and m/z = 44 mass spectrometry signals, which is calculated by flowing CO_2 at concentrations of 15, 7.5 and 5 vol%, balanced with Ar in an empty reactor at room temperature.

The carbon monoxide selectivity (S_{CO}) and CH_4 and CO_2 conversion (X_{CH_4} and X_{CO_2} respectively) were calculated as follows, where n_{CO}, n_{CH_4} and n_{CO_2} are the moles of CO, CH_4 and CO_2 as integrated with time for the CO, CH_4 and CO_2 profiles respectively:

$$S_{CO} = \frac{n_{CO}}{n_{CO} + n_{CO_2}} \quad (6)$$

$$X_{CH_4} = \frac{n_{CH_{4,in}} - n_{CH_{4,out}}}{n_{CH_{4,in}}} \quad (7)$$

$$X_{CO_2} = \frac{n_{CO_{2,in}} - n_{CO_{2,out}}}{n_{CO_{2,in}}} \quad (8)$$

The oxygen supply capacity was calculated using the following equation, adapted from ref. 30:

$$\zeta = \frac{n_{H_2}}{m} \times M_{ceria} \quad (9)$$

where ζ is the oxygen supply capacity of the oxide in mol O mol_{oxide}^{-1}, n_{H_2} is the H_2 moles consumed by the oxide determined by TPR analyses, m is the mass of the sample measured by TPR, and M_{ceria} is the molecular mass of the cerium oxides tested.

Conflicts of interest

The authors declare no conflict of interest.

Acknowledgements

AJC and MB would like to acknowledge the support of Juan de la Cierva fellowships by the Spanish Ministry of Science (grant numbers FJCI-2017-33967 and IJCI-2017-34110). We acknowledge the support of the Electronic Microscopy Service of the Universitat Politècnica de València.

References

1 A. Thursfield, A. Murugan, R. Franca and I. S. Metcalfe, *Energy Environ. Sci.*, 2012, **5**, 7421–7459.
2 X. Zhu, F. Donat, Q. Imtiaz, C. R. Müller and F. Li, *Energy Environ. Sci.*, 2020, **14**, 112.
3 J. Garcia-Fayos, J. M. Serra, M. W. J. Luiten-Olieman and W. A. Meulenberg, *Gas separation ceramic membranes*, 2020.
4 A. J. Carrillo, J. L. M. Rupp and J. M. Coronado, in *Energy Storage and Conversion Materials*, ed. S. J. Skinner, The Royal Society of Chemistry, Inorganic, 2020, pp. 136–187.
5 V. P. Haribal, X. Wang, R. Dudek, C. Paulus, B. Turk, R. Gupta and F. Li, *Adv. Energy Mater.*, 2019, **9**, 1901963.
6 P. T. Krenzke, J. R. Fosheim and J. H. Davidson, *Sol. Energy*, 2017, **156**, 48–72.
7 C. Agrafiotis, H. Von Storch, M. Roeb and C. Sattler, *Renewable Sustainable Energy Rev.*, 2014, **29**, 656–682.
8 J. Zhang, V. Haribal and F. Li, *Sci. Adv.*, 2017, **3**, e1701184.
9 K. J. Warren, R. J. Carrillo, B. Greek, C. M. Hill and J. R. Scheffe, *Energy Technol.*, 2020, **8**, 2000053.
10 R. J. Carrillo and J. R. Scheffe, *Sol. Energy*, 2017, **156**, 3–20.
11 K. J. Warren, J. Reim, K. Randhir, B. Greek, R. Carrillo, D. W. Hahn and J. R. Scheffe, *Energy Technol.*, 2017, **5**, 2138–2149.
12 M. Welte, K. Warren, J. R. Scheffe and A. Steinfeld, *Ind. Eng. Chem. Res.*, 2017, **56**, 10300–10308.
13 S. Chuayboon, S. Abanades and S. Rodat, *Chem. Eng. J.*, 2019, **356**, 756–770.
14 Y. Zheng, X. Zhu, H. Wang, K. Li, Y. Wang and Y. Wei, *J. Rare Earths*, 2014, **32**, 842–848.
15 X. Gao, A. Vidal, A. Bayon, R. Bader, J. Hinkley, W. Lipiński and A. Tricoli, *J. Mater. Chem. A*, 2016, **4**, 9614–9624.
16 Y. Chen, X. Zhu, K. Li, Y. Wei, Y. Zheng and H. Wang, *ACS Sustainable Chem. Eng.*, 2019, **7**, 15452–15462.
17 X. Gao, G. Liu, Y. Zhu, P. Kreider, A. Bayon, T. Gengenbach, T. Lu, Y. Liu, J. Hinkley, W. Lipiński and A. Tricoli, *Nano Energy*, 2018, **50**, 347–358.
18 X. Gao, I. Di Bernardo, P. Kreider, T. Tran-Phu, X. Cai, N. Wang, Y. Zhu, M. B. Venkataraman, J. Lipton-Duffin, A. Bayon, W. Lipiński and A. Tricoli, *ACS Catal.*, 2019, 9880–9890.
19 M. Fathi, E. Bjorgum, T. Viig and O. Rokstad, *Catal. Today*, 2000, **63**, 489–497.

20 C. Ruan, Z.-Q. Huang, J. Lin, L. Li, X. Liu, M. Tian, C. Huang, C.-R. Chang, J. Li and X. Wang, *Energy Environ. Sci.*, 2019, **12**, 767–779.
21 T. W. Hansen, A. T. DeLaRiva, S. R. Challa and A. K. Datye, *Acc. Chem. Res.*, 2013, **46**, 1720–1730.
22 D. Neagu, G. Tsekouras, D. N. Miller, H. Menard and J. T. Irvine, *Nat. Chem.*, 2013, **5**, 916–923.
23 D. Neagu, T. S. Oh, D. N. Miller, H. Menard, S. M. Bukhari, S. R. Gamble, R. J. Gorte, J. M. Vohs and J. T. Irvine, *Nat. Commun.*, 2015, **6**, 8120.
24 J. T. S. Irvine, D. Neagu, M. C. Verbraeken, C. Chatzichristodoulou, C. Graves and M. B. Mogensen, *Nat. Energy*, 2016, **1**, 15014.
25 B. Hua, M. Li, Y. F. Sun, J. H. Li and J. L. Luo, *ChemSusChem*, 2017, **10**, 3333–3341.
26 K. Kousi, D. Neagu, L. Bekris, E. I. Papaioannou and I. S. Metcalfe, *Angew. Chem., Int. Ed.*, 2020, **59**, 2510–2519.
27 M. A. Naeem, P. M. Abdala, A. Armutlulu, S. M. Kim, A. Fedorov and C. R. Müller, *ACS Catal.*, 2020, **10**, 1923–1937.
28 Y. J. Wong, M. K. Koh, N. F. Khairudin, S. Ichikawa, Y. Morikawa and A. R. Mohamed, *ChemCatChem*, 2019, **11**, 5593–5605.
29 S. Vecino-Mantilla, P. Gauthier-Maradei, M. Huvé, J. M. Serra, P. Roussel and G. H. Gauthier, *ChemCatChem*, 2019, **11**, 4631–4641.
30 K. Kousi, D. Neagu, L. Bekris, E. Calì, G. Kerherve, E. I. Papaioannou, D. J. Payne and I. S. Metcalfe, *J. Mater. Chem. A*, 2020, **8**, 12406–12417.
31 G. Dimitrakopoulos, A. F. Ghoniem and B. Yildiz, *Sustainable Energy Fuels*, 2019, **3**, 2347–2355.
32 A. J. Carrillo, K. J. Kim, Z. D. Hood, A. H. Bork and J. L. M. Rupp, *ACS Appl. Energy Mater.*, 2020, 1–34.
33 T. Montini, M. Melchionna, M. Monai and P. Fornasiero, *Chem. Rev.*, 2016, **116**, 5987–6041.
34 Y. Chen, B. DeGlee, Y. Tang, Z. Wang, B. Zhao, Y. Wei, L. Zhang, S. Yoo, K. Pei, J. H. Kim, Y. Ding, P. Hu, F. F. Tao and M. Liu, *Nat. Energy*, 2018, **3**, 1042–1050.
35 X. Shen, T. Chen, S. R. Bishop, N. H. Perry, H. L. Tuller and K. Sasaki, *J. Power Sources*, 2017, **370**, 122–130.
36 J. M. Serra, J. F. Borrás-Morell, B. García-Baños, M. Balaguer, P. Plaza-González, J. Santos-Blasco, D. Catalán-Martínez, L. Navarrete and J. M. Catalá-Civera, *Nat. Energy*, 2020, **5**, 910–919.
37 R. D. Shannon, *Acta Crystallogr., Sect. A: Cryst. Phys., Diffr., Theor. Gen. Crystallogr.*, 1976, **32**, 751–767.
38 P. Singh and M. S. Hegde, *Chem. Mater.*, 2009, **21**, 3337–3345.
39 S. Sharma, Z. Hu, P. Zhang, E. W. McFarland and H. Metiu, *J. Catal.*, 2011, **278**, 297–309.
40 R. Schmitt, A. Nenning, O. Kraynis, R. Korobko, A. I. Frenkel, I. Lubomirsky, S. M. Haile and J. L. M. Rupp, *Chem. Soc. Rev.*, 2020, **49**, 554–592.
41 E. Sediva, A. J. Carrillo, C. E. Halloran and J. L. M. Rupp, *ACS Appl. Energy Mater.*, 2021, **4**, 1474–1483.
42 H. Han, J. Park, S. Y. Nam, K. J. Kim, G. M. Choi, S. S. P. Parkin, H. M. Jang and J. T. S. Irvine, *Nat. Commun.*, 2019, **10**, 1471.
43 C. L. Muhich, *J. Phys. Chem. C*, 2017, **121**, 8052–8059.
44 C. Solís, M. Balaguer and J. M. Serra, *Membranes*, 2020, **10**, 1–16.
45 M. Balaguer, C. Solís and J. M. Serra, *Chem. Mater.*, 2011, **23**, 2333–2343.
46 M. Balaguer, C. Solís, S. Roitsch and J. M. Serra, *Dalton Trans.*, 2014, **43**, 4305–4312.
47 Y. Gao, D. Chen, M. Saccoccio, Z. Lu and F. Ciucci, *Nano Energy*, 2016, **27**, 499–508.
48 J. Spring, E. Sediva, Z. D. Hood, J. C. Gonzalez-Rosillo, W. O'Leary, K. J. Kim, A. J. Carrillo and J. L. M. Rupp, *Small*, 2020, **16**, 2003224.
49 D. Neagu, V. Kyriakou, I. Roiban, M. Aouine, C. Tang, A. Caravaca, K. Kousi, I. Schreur-Piet, I. S. Metcalfe, P. Vernoux, M. C. M. van de Sanden and M. N. Tsampas, *ACS Nano*, 2019, **13**, 12996–13005.
50 J. Moulder, W. Stickle, P. Sobol and K. Bomben, *Handbook of X-ray photoelectron spectroscopy*, 1992.
51 C. Yang, X. Yu, S. Heißler, A. Nefedov, S. Colussi, J. Llorca, A. Trovarelli, Y. Wang and C. Wöll, *Angew. Chem., Int. Ed.*, 2017, **56**, 375–379.
52 E. Bêche, P. Charvin, D. Perarnau, S. Abanades and G. Flamant, *Surf. Interface Anal.*, 2008, **40**, 264–267.
53 J. F. Moulder, *Handbook of X-ray photoelectron spectroscopy, physical electronics*, 1995.
54 P. T. Krenzke, J. R. Fosheim, J. Zheng and J. H. Davidson, *Int. J. Hydrogen Energy*, 2015, **41**, 12799–12811.
55 K. J. Warren and J. R. Scheffe, *J. Phys. Chem. C*, 2019, **123**, 13208–13218.
56 S. Ackermann, L. Sauvin, R. Castiglioni, J. L. M. Rupp, J. R. Scheffe and A. Steinfeld, *J. Phys. Chem. C*, 2015, **119**, 16452–16461.
57 D. Sastre, D. P. Serrano, P. Pizarro and J. M. Coronado, *J. CO_2 Util.*, 2019, **31**, 16–26.